Journal of Computational Physics 282 (2015) 345–359

Contents lists available at ScienceDirect

Journal of Computational Physics

www.elsevier.com/locate/jcp

Finite element approximation of the radiative transport equation in a medium with piece-wise constant refractive index

O. Lehtikangas [a,*], T. Tarvainen [a,b], A.D. Kim [c], S.R. Arridge [b]

[a] Department of Applied Physics, University of Eastern Finland, PO Box 1627, 70211 Kuopio, Finland
[b] Department of Computer Science, University College London, Gower Street, London WC1E 6BT, United Kingdom
[c] Applied Mathematics Unit, School of Natural Sciences, University of California, Merced, CA 95343, USA

ARTICLE INFO

Article history:
Received 3 January 2014
Received in revised form 4 November 2014
Accepted 23 November 2014
Available online 27 November 2014

Keywords:
Radiative transport equation
Refractive index
Finite element method

ABSTRACT

The radiative transport equation can be used as a light transport model in a medium with scattering particles, such as biological tissues. In the radiative transport equation, the refractive index is assumed to be constant within the medium. However, in biomedical media, changes in the refractive index can occur between different tissue types. In this work, light propagation in a medium with piece-wise constant refractive index is considered. Light propagation in each sub-domain with a constant refractive index is modeled using the radiative transport equation and the equations are coupled using boundary conditions describing Fresnel reflection and refraction phenomena on the interfaces between the sub-domains. The resulting coupled system of radiative transport equations is numerically solved using a finite element method. The approach is tested with simulations. The results show that this coupled system describes light propagation accurately through comparison with the Monte Carlo method. It is also shown that neglecting the internal changes of the refractive index can lead to erroneous boundary measurements of scattered light.
© 2014 The Authors. Published by Elsevier Inc. This is an open access article under the CC BY-NC-ND license (http://creativecommons.org/licenses/by-nc-nd/3.0/).

1. Introduction

The radiative transport equation (RTE) can be used to model propagation of particles such as neutrons and photons in a scattering medium [1–3]. Applications can be found in atmospheric and ocean optics [4], astrophysics [5], nuclear reactor physics [6] and biomedical optics [7]. In biomedical diffuse optical tomography (DOT), images of the optical properties of the target are reconstructed from measurements of near-infrared light made on the surface of the target. The image reconstruction procedure in DOT requires a model for light propagation inside the target in which the RTE can be utilized [8–11].

The RTE takes into account absorption and multiple scattering inside tissues and treats photons as particles which propagate along straight lines between scattering and absorption events. The refractive index is assumed to be a constant inside tissues. However, the refractive index can change between different tissue types inside the target even though these changes are typically neglected in DOT.

* Corresponding author. Tel.: +358 40 3553913; fax: +358 17 162585.
E-mail address: Ossi.Lehtikangas@uef.fi (O. Lehtikangas).

http://dx.doi.org/10.1016/j.jcp.2014.11.025
0021-9991/© 2014 The Authors. Published by Elsevier Inc. This is an open access article under the CC BY-NC-ND license (http://creativecommons.org/licenses/by-nc-nd/3.0/).

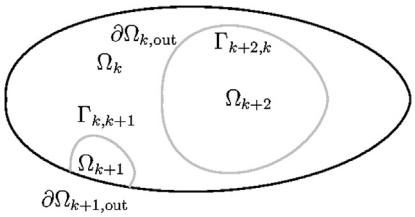

Fig. 1. A sketch of sub-domains having different refractive indices. The interfaces Γ between the sub-domains are marked with gray color and the outer boundaries $\partial\Omega_{\text{out}}$ with black color.

A more general version of the RTE with a spatially dependent refractive index was derived in [12], and more recently investigated in [13–21]. This model allows curved photon paths between absorption and scattering events based on the gradient field of the refractive index. Therefore, the refractive index is assumed to be a smooth continuous function such that the gradient is well defined. However, in biomedical applications the refractive index can have jumps between different tissue types, such as between skull and cerebrospinal fluid in the brain, and a smooth function may not approximate these jumps correctly.

The RTE with piecewise constant refractive index with Fresnel reflection and transmission between the regions has been considered in [22–28]. The approach was developed for a one dimensional spherically symmetric case in [22,23] and for multilayered media in [24–27]. Furthermore, a one dimensional plane parallel geometry with multilayered media was considered in [28]. In this paper, this approach is extended to general geometry. Light propagation in each sub-domain with a constant refractive index is modeled using the RTE and the equations are coupled using boundary conditions describing Fresnel reflection and transmission on the interfaces between the sub-domains. This leads to a coupled system of radiative transport equations (cRTE).

In the numerical solution of the RTE, different discretization methods have been applied for both the spatial and angular parts of the solution. For the spatial part, a finite difference method [29–31], a finite element method (FEM) [32–35] and a finite volume method [36–38] have been the most commonly applied approaches. For the angular part, a discrete ordinate method [29–31,33,36,38], the FEM [34,35,39–41] and a spherical harmonics method (P_n) [42–45] have been utilized.

In this work, the cRTE is numerically solved using the FEM both in the space and in the angle. In the approach, the boundary conditions are formulated in a general form. Hence, the model is applicable in complex geometries represented by finite element meshes with an arbitrary number of sub-domains and inhomogeneous parameter distributions. Moreover, using the FEM for the angular part enables an accurate and simple implementation of the boundary conditions.

The rest of the paper is organized as follows. In Section 2, the RTE and the boundary conditions between piece-wise constant regions of refractive index are reviewed and the coupled system of RTEs is described. In Section 3, the numerical approximation of the coupled system of the RTEs using the FEM is described. In Section 4, simulation results are shown. Section 5 gives the conclusions.

2. Radiative transport equation with piece-wise constant refractive index

Let $\Omega \subset \mathbb{R}^d$ be the physical domain with a boundary $\partial\Omega$, and $d = 2, 3$ be the dimension of the domain. In addition, let $\hat{\mathbf{s}} \in \mathbb{S}^{d-1}$ denote a unit vector in the direction of interest on the unit sphere $\mathbb{S}^{d-1}$. Let the refractive index n be a piece-wise constant within N disjoint sub-domains Ω_k, $k = 1, \ldots, N$. An interface between the sub-domains Ω_k and Ω_n with different refractive indices n_k and n_n is denoted by $\Gamma_{k,n} = \partial\Omega_k \cap \partial\Omega_n$ as shown in Fig. 1. Further, the union of the interfaces of the sub-domain Ω_k can be written as $\Gamma_k = \bigcup_{n=1,n\neq k}^{N} \Gamma_{k,m}$. With these notations, the boundary of the sub-domain Ω_k can be divided into the outer boundary and the union of the interfaces $\partial\Omega_k = \partial\Omega_{k,\text{out}} \cup \Gamma_k$. Light propagation in each sub-domain Ω_k can be modeled using the RTE and the equations are coupled using the boundary conditions at the interfaces $\Gamma_{k,n}$.

2.1. Radiative transport equation

The frequency domain version of the RTE in the sub-domain Ω_k can be written as [8]

$$\left(\frac{\mathrm{i}\omega}{c_k} + \hat{\mathbf{s}} \cdot \nabla + \mu_{\mathrm{a}}\right)\phi_k(\mathbf{r}, \hat{\mathbf{s}}) = \mu_{\mathrm{s}}\mathcal{L}\phi_k(\mathbf{r}, \hat{\mathbf{s}}) \tag{1}$$

where i is the imaginary unit, ω is the angular modulation frequency of the input signal, $c_k = c_0/n_k$ is the speed of light in the sub-domain Ω_k, c_0 is the speed of light in a vacuum, $\phi_k(\mathbf{r}, \hat{\mathbf{s}})$ is the radiance in the sub-domain Ω_k, and $\mu_{\mathrm{s}} = \mu_{\mathrm{s}}(\mathbf{r})$ and $\mu_{\mathrm{a}} = \mu_{\mathrm{a}}(\mathbf{r})$ are the scattering and absorption coefficients of the medium, respectively [1,2]. The scattering operator $\mathcal{L}$ is

$$\mathcal{L}\phi_k(\mathbf{r}, \hat{\mathbf{s}}) = -\phi_k(\mathbf{r}, \hat{\mathbf{s}}) + \int_{\mathbb{S}^{d-1}} \Theta\left(\hat{\mathbf{s}} \cdot \hat{\mathbf{s}}'\right)\phi_k\left(r, \hat{\mathbf{s}}'\right)\mathrm{d}\hat{\mathbf{s}}'. \tag{2}$$

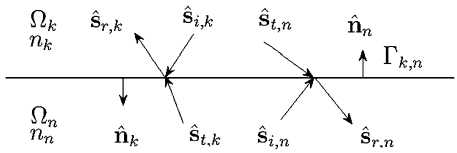

Fig. 2. Interface $\Gamma_{k,n}$ between the sub-domains Ω_k and Ω_n with different refractive indices n_k and n_n. The direction of incoming radiance to the interface is denoted by $\hat{\mathbf{s}}_i$, the direction of reflected radiance by $\hat{\mathbf{s}}_r$ and the direction of radiance which transmits through the interface is denoted by $\hat{\mathbf{s}}_t$. Outward unit normal is denoted by $\hat{\mathbf{n}}$.

The scattering phase function $\Theta(\hat{\mathbf{s}}\cdot\hat{\mathbf{s}}')$ describes the probability for a photon with an initial direction $\hat{\mathbf{s}}'$ to scatter in a direction $\hat{\mathbf{s}}$. In this work, the Henyey–Greenstein scattering function [46] is used

$$\Theta\left(\hat{\mathbf{s}}\cdot\hat{\mathbf{s}}'\right)=\frac{1}{|\mathbb{S}^{d-1}|}\frac{1-g^2}{(1+g^2-2g\hat{\mathbf{s}}\cdot\hat{\mathbf{s}}')^{d/2}}, \tag{3}$$

where $g\in[-1,1]$ is the anisotropy parameter defining the shape of the probability distribution. In biological tissues, g is typically close to one indicating that scattering is forward-peaked. Further, $|\mathbb{S}^{d-1}|$ is the surface measure of $\mathbb{S}^{d-1}$ ($|\mathbb{S}^1|=2\pi$ and $|\mathbb{S}^2|=4\pi$). The fluence is defined as an integral of the radiance over the angular directions [8]

$$\Phi_k(\mathbf{r})=\int_{\mathbb{S}^{d-1}}\phi_k(\mathbf{r},\hat{\mathbf{s}})\mathrm{d}\hat{\mathbf{s}}. \tag{4}$$

2.2. Boundary conditions

The boundary condition in the sub-domain Ω_k at the interface $\Gamma_{k,n}$ in an inward direction $\hat{\mathbf{s}}_{r,k}$ takes into account the reflected radiance from a direction $\hat{\mathbf{s}}_{i,k}$ and the transmitted radiance from the sub-domain Ω_n from a direction $\hat{\mathbf{s}}_{t,k}$ as shown in Fig. 2. The boundary condition can be written as

$$\phi_k(\mathbf{r},\hat{\mathbf{s}})=R_{k,n}\phi_k\left(\mathbf{r},H_k^{-1}\hat{\mathbf{s}}\right)+T_{n,k}\phi_n\left(\mathbf{r},K_{n,k}^{-1}(\hat{\mathbf{s}})\right),\quad \mathbf{r}\in\Gamma_{k,n},\quad \hat{\mathbf{s}}\cdot\hat{\mathbf{n}}_k<0, \tag{5}$$

where $R_{k,n}=R_{k,n}(\hat{\mathbf{s}}_{i,k},\hat{\mathbf{n}}_k,n_k,n_k)$ is the Fresnel reflection coefficient between the sub-domains Ω_k and Ω_n

$$R_{k,n}=\frac{1}{2}\left(\frac{n_k\cos\theta_k-n_n\cos\theta_n}{n_k\cos\theta_k+n_n\cos\theta_n}\right)^2+\frac{1}{2}\left(\frac{n_k\cos\theta_n-n_n\cos\theta_k}{n_k\cos\theta_n+n_n\cos\theta_k}\right)^2, \tag{6}$$

where

$$\cos\theta_k=\hat{\mathbf{n}}_k\cdot\hat{\mathbf{s}}_{i,k}, \tag{7}$$

$$\cos\theta_n=\sqrt{1-\left(\frac{n_k}{n_n}\right)^2\left(1-(\cos\theta_k)^2\right)}. \tag{8}$$

Further, $T_{n,k}$ is the Fresnel transmission coefficient between the sub-domains Ω_n and Ω_k

$$T_{n,k}=1-R_{n,k}. \tag{9}$$

Fig. 3 shows the Fresnel reflection coefficient R and the transmission coefficient T as a function of an incident angle.

The mapping H_k^{-1} is the inverse reflection law giving the initial direction of the radiance $\hat{\mathbf{s}}_{i,k}$ for a given direction of the reflected radiance $\hat{\mathbf{s}}_{r,k}$. The reflection law can be written in a vector form as $H_k:\hat{\mathbf{s}}_{i,k}\to\hat{\mathbf{s}}_{r,k}$

$$\hat{\mathbf{s}}_{r,k}=H_k\hat{\mathbf{s}}_{i,k}, \tag{10}$$

$$H_k=\left(\mathbf{I}-2\hat{\mathbf{n}}_k\hat{\mathbf{n}}_k^T\right), \tag{11}$$

where $\mathbf{I}$ is an identity matrix. The inverse reflection law H_k^{-1} can be computed

$$\hat{\mathbf{s}}_{i,k}=H_k^{-1}\hat{\mathbf{s}}_{r,k}=H_k\hat{\mathbf{s}}_{r,k}, \tag{12}$$

since the matrix H_k is a Householder transformation and thus $H_k^{-1}=H_k$.

The mapping $K_{n,k}^{-1}$ is the inverse Snell's law giving the direction $\hat{\mathbf{s}}_{t,k}$ from which the radiance is transmitted from the sub-domain Ω_n into the sub-domain Ω_k for a given direction $\hat{\mathbf{s}}_{r,k}$. The Snell's law for the refraction of the radiance between the sub-domains Ω_n and Ω_k can be written in a vector form $K_{n,k}:(\hat{\mathbf{s}}_{t,k},\hat{\mathbf{n}}_n,n_n,n_k)\to\hat{\mathbf{s}}_{r,k}$

$$\hat{\mathbf{s}}_{r,k}=\frac{n_n}{n_k}\hat{\mathbf{s}}_{t,k}+\left(\cos\varphi_k-\frac{n_n}{n_k}\cos\varphi_n\right)\hat{\mathbf{n}}_n, \tag{13}$$

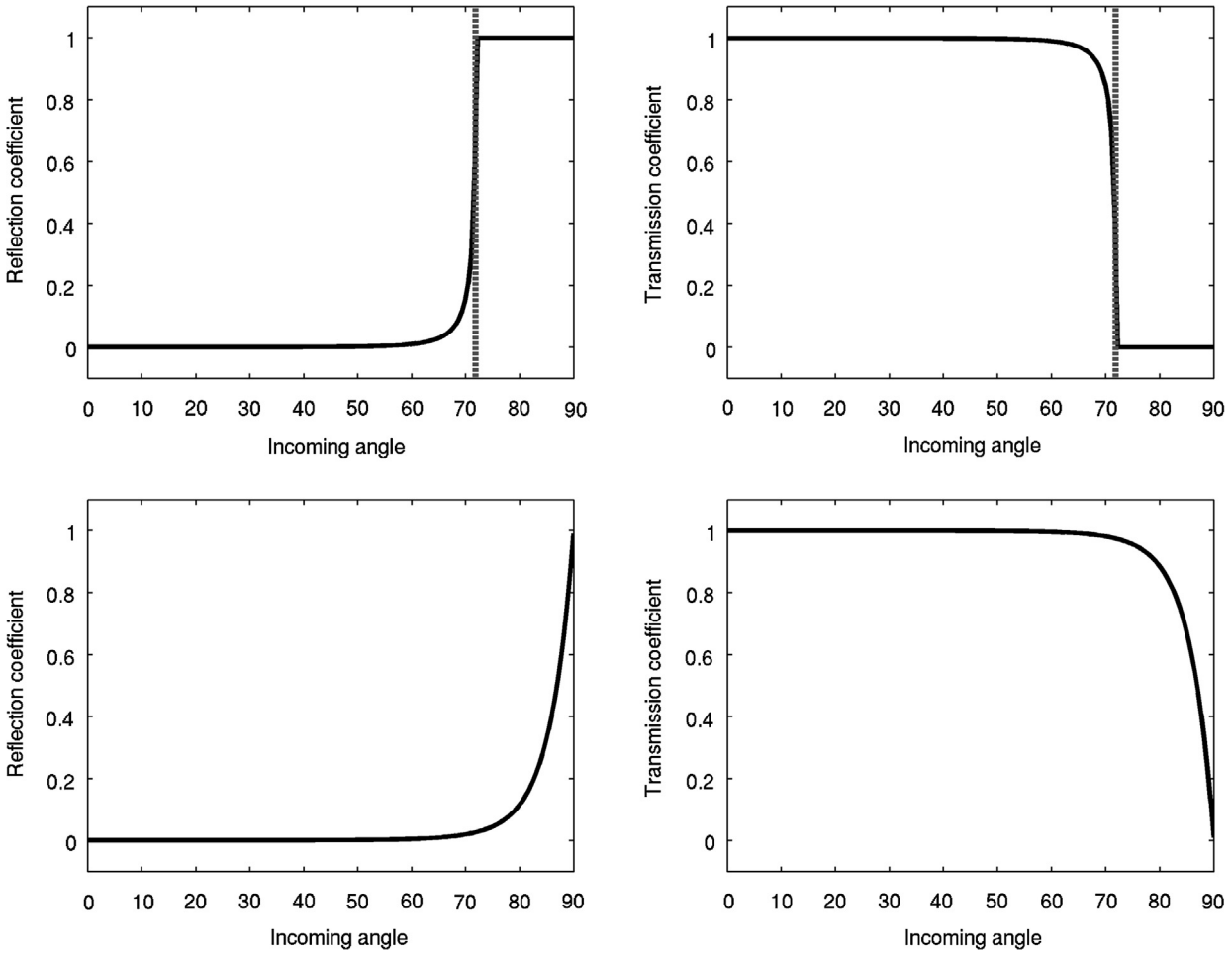

Fig. 3. Fresnel reflection coefficient R (left column) and transmission coefficient T (right column) between sub-domains with refractive indices $n_1 = 1.4$ and $n_2 = 1.33$ (top row) and refractive indices $n_1 = 1.33$ and $n_2 = 1.4$ (bottom row) as a function of incoming angle. The critical angle $\theta_{\text{crit}} = \sin^{-1}(n_2/n_1)$ is marked with a gray vertical line when total internal reflection occurs.

where

$$\cos\varphi_n = \hat{\mathbf{n}}_n \cdot \hat{\mathbf{s}}_{t,k}, \tag{14}$$

$$\cos\varphi_k = \sqrt{1 - \left(\frac{n_n}{n_k}\right)^2 \left(1 - (\cos\varphi_n)^2\right)}. \tag{15}$$

The inverse Snell's law $K_{n,k}^{-1} : (\hat{\mathbf{s}}_{r,k}, \hat{\mathbf{n}}_n, n_n, n_k) \to \hat{\mathbf{s}}_{t,k}$ can be computed as $K_{n,k} : (-\hat{\mathbf{s}}_{r,k}, -\hat{\mathbf{n}}_n, n_k, n_n) \to -\hat{\mathbf{s}}_{t,k}$ due to the reciprocity principle of light propagation.

The boundary condition for the outer boundary in the sub-domain Ω_k takes into account a boundary source $\phi_{0,k}(\mathbf{r}, \hat{\mathbf{s}})$ and the reflection of the radiance due to a mismatch in refractive indices at the outer boundary

$$\phi_k(\mathbf{r}, \hat{\mathbf{s}}) = \phi_{0,k}(\mathbf{r}, \hat{\mathbf{s}}) + R_{k,\text{out}}\phi_k(\mathbf{r}, H_k\hat{\mathbf{s}}), \quad \mathbf{r} \in \partial\Omega_{k,\text{out}}, \quad \hat{\mathbf{s}} \cdot \hat{\mathbf{n}}_k < 0, \tag{16}$$

where $R_{k,\text{out}} = R_{k,\text{out}}(\hat{\mathbf{s}}_{i,k}, \hat{\mathbf{n}}_k, n_k, n_{\text{out}})$ is the reflection coefficient between the sub-domain Ω_k and the exterior of the domain Ω with the refractive index n_{out}.

2.3. Coupled system of radiative transport equations

The coupled system of RTEs for N sub-domains with different refractive indices can be written as

$$\left(\frac{\mathrm{i}\omega}{c_k} + \hat{\mathbf{s}} \cdot \nabla + \mu_{\text{a}}\right)\phi_k(\mathbf{r}, \hat{\mathbf{s}}) = \mu_{\text{s}}\mathcal{L}\phi_k(\mathbf{r}, \hat{\mathbf{s}}), \quad \mathbf{r} \in \Omega_k \tag{17a}$$

$$\phi_k(\mathbf{r}, \hat{\mathbf{s}}) = \phi_{0,k}(\mathbf{r}, \hat{\mathbf{s}}) + R_{k,\text{out}}\phi_k(\mathbf{r}, H_k\hat{\mathbf{s}}), \quad \mathbf{r} \in \partial\Omega_{k,\text{out}}, \quad \hat{\mathbf{s}} \cdot \hat{\mathbf{n}}_k, < 0, \tag{17b}$$

$$\phi_k(\mathbf{r},\hat{\mathbf{s}}) = R_{k,n}\phi_k(\mathbf{r}, H_k\hat{\mathbf{s}}) + T_{n,k}\phi_n\big(\mathbf{r}, K_{n,k}^{-1}(\hat{\mathbf{s}})\big), \quad \mathbf{r}\in\Gamma_{k,n}, \quad \hat{\mathbf{s}}\cdot\hat{\mathbf{n}}_k < 0,$$
$$n,k = 1,\dots,N. \tag{17c}$$

3. Finite element approximation of the coupled system

In this work, the solution of the cRTE (17) is numerically approximated using the FEM. In the FEM, a variational formulation of the original problem is derived, and then this infinite dimensional problem is discretized using a suitable set of basis functions.

To derive the variational formulation of the coupled system, we follow a similar procedure as in [34,47–50]. Thus, first each of the equations in (17a) are multiplied by a test function v_k and integrated over the domain $\Omega_k\times\mathbb{S}^{d-1}$. Then, by using the Green's theorem [51], separating the resulting boundary integrals over the outer boundary $\partial\Omega_{k,\text{out}}$ and over the interfaces $\Gamma_{k,n}$, and utilizing the boundary conditions (17b) and (17c), the variational formulation is obtained. The variational formulation of the cRTE (17) with a streamline diffusion modification [32,48,52] can be written as

$$\begin{aligned}
&\sum_{k=1}^{N}\Bigg(\int_{\Omega_k}\int_{\mathbb{S}^{d-1}}\frac{\mathrm{i}\omega}{c_k}\phi_k(\mathbf{r},\hat{\mathbf{s}})v_k(\mathbf{r},\hat{\mathbf{s}})\mathrm{d}\hat{\mathbf{s}}\mathrm{d}\mathbf{r} - \int_{\Omega_k}\int_{\mathbb{S}^{d-1}}\hat{\mathbf{s}}\cdot\nabla v_k(\mathbf{r},\hat{\mathbf{s}})\phi_k(\mathbf{r},\hat{\mathbf{s}})\mathrm{d}\hat{\mathbf{s}}\mathrm{d}\mathbf{r}\\
&+\int_{\partial\Omega_k}\int_{\mathbb{S}^{d-1}}(\hat{\mathbf{s}}\cdot\hat{\mathbf{n}}_k)_+\phi_k(\mathbf{r},\hat{\mathbf{s}})v_k(\mathbf{r},\hat{\mathbf{s}})\mathrm{d}\hat{\mathbf{s}}\mathrm{d}S - \int_{\partial\Omega_{k,\text{out}}}\int_{\mathbb{S}^{d-1}}(\hat{\mathbf{s}}\cdot\hat{\mathbf{n}}_k)_-R_{k,\text{out}}\phi_k(\mathbf{r},H_k\hat{\mathbf{s}})v_k(\mathbf{r},\hat{\mathbf{s}})\mathrm{d}\hat{\mathbf{s}}\mathrm{d}S\\
&-\sum_{n=1,n\neq k}^{N}\int_{\Gamma_{k,n}}\int_{\mathbb{S}^{d-1}}(\hat{\mathbf{s}}\cdot\hat{\mathbf{n}}_k)_-R_{k,n}\phi_k(\mathbf{r},H_k\hat{\mathbf{s}})v_k(\mathbf{r},\hat{\mathbf{s}})\mathrm{d}\hat{\mathbf{s}}\mathrm{d}S\\
&-\sum_{n=1,n\neq k}^{N}\int_{\Gamma_{k,n}}\int_{\mathbb{S}^{d-1}}(\hat{\mathbf{s}}\cdot\hat{\mathbf{n}}_k)_-T_{n,k}\phi_n\big(\mathbf{r},K_{n,k}^{-1}(\hat{\mathbf{s}})\big)v_k(\mathbf{r},\hat{\mathbf{s}})\mathrm{d}\hat{\mathbf{s}}\mathrm{d}S + \int_{\Omega_k}\int_{\mathbb{S}^{d-1}}\mu_\mathrm{a}\phi_k(\mathbf{r},\hat{\mathbf{s}})v_k(\mathbf{r},\hat{\mathbf{s}})\mathrm{d}\hat{\mathbf{s}}\mathrm{d}\mathbf{r}\\
&-\int_{\Omega_k}\int_{\mathbb{S}^{d-1}}\mathcal{L}\phi_k(\mathbf{r},\hat{\mathbf{s}})v_k(\mathbf{r},\hat{\mathbf{s}})\mathrm{d}\hat{\mathbf{s}}\mathrm{d}\mathbf{r} + \int_{\Omega_k}\int_{\mathbb{S}^{d-1}}\delta\frac{\mathrm{i}\omega}{c}\phi_k(\mathbf{r},\hat{\mathbf{s}})\hat{\mathbf{s}}\cdot\nabla v_k(\mathbf{r},\hat{\mathbf{s}})\mathrm{d}\hat{\mathbf{s}}\mathrm{d}\mathbf{r}\\
&+\int_{\Omega_k}\int_{\mathbb{S}^{d-1}}\delta\big(\hat{\mathbf{s}}\cdot\nabla\phi_k(\mathbf{r},\hat{\mathbf{s}})\big)\big(\hat{\mathbf{s}}\cdot\nabla v_k(\mathbf{r},\hat{\mathbf{s}})\big)\mathrm{d}\hat{\mathbf{s}}\mathrm{d}\mathbf{r} + \int_{\Omega_k}\int_{\mathbb{S}^{d-1}}\delta\mu_\mathrm{a}\phi_k(\mathbf{r},\hat{\mathbf{s}})v_k(\mathbf{r},\hat{\mathbf{s}})\mathrm{d}\hat{\mathbf{s}}\mathrm{d}\mathbf{r}\\
&-\int_{\Omega_k}\delta\int_{\mathbb{S}^{d-1}}\mathcal{L}\phi_k(\mathbf{r},\hat{\mathbf{s}})\big(\hat{\mathbf{s}}\cdot\nabla v_k(\mathbf{r},\hat{\mathbf{s}})\big)\mathrm{d}\hat{\mathbf{s}}\mathrm{d}\mathbf{r} - \int_{\partial\Omega_{k,\text{out}}}\int_{\mathbb{S}^{d-1}}(\hat{\mathbf{s}}\cdot\hat{\mathbf{n}}_k)_-\phi_{0,k}(\mathbf{r},\hat{\mathbf{s}})v_k(\mathbf{r},\hat{\mathbf{s}})\mathrm{d}\hat{\mathbf{s}}\mathrm{d}S\Bigg) = 0
\end{aligned} \tag{18}$$

where δ is a streamline-diffusion modification parameter and $(\hat{\mathbf{s}}\cdot\hat{\mathbf{n}}_k)_+$ and $(\hat{\mathbf{s}}\cdot\hat{\mathbf{n}}_k)_-$ denote the positive and negative parts of the function $(\hat{\mathbf{s}}\cdot\hat{\mathbf{n}}_k)$.

The FE-approximation is obtained by approximating the solutions $\phi_k(\mathbf{r},\hat{\mathbf{s}})$ of the variational formulation (18) with a linear combination of the basis functions

$$\phi_k(\mathbf{r},\hat{\mathbf{s}}) \approx \sum_{i=1}^{N_{s,k}}\sum_{l=1}^{N_{a,k}}\alpha_{il}^k\psi_{i,k}(\mathbf{r})\psi_{l,k}(\hat{\mathbf{s}}), \tag{19}$$

where $\psi_{i,k}(\mathbf{r})$ and $\psi_{l,k}(\hat{\mathbf{s}})$ are the nodal basis functions of the spatial and angular discretizations of $\Omega_k\times\mathbb{S}^{d-1}$, α_{il}^k is the radiance in spatial nodal point i into angular direction l in the sub-domain Ω_k, and $N_{s,k}$ and $N_{a,k}$ are the number of spatial and angular nodes in the sub-domain Ω_k, respectively. Therefore, different number of angular directions can be used in different sub-domains if that is feasible. In this work, we use a piecewise linear basis for both spatial and angular parts of the solution. The FE-approximation of the coupled model can be written in a matrix form as

$$\begin{pmatrix} A_1 & C_{1,2} & \cdots & \cdots & C_{1,N}\\ C_{2,1} & A_2 & \ddots & \ddots & \vdots\\ \vdots & \ddots & \ddots & \ddots & \vdots\\ C_{N-1,1} & \ddots & \ddots & A_{N-1} & C_{N-1,N}\\ C_{N,1} & \cdots & \cdots & C_{N,N-1} & A_N \end{pmatrix}\begin{pmatrix}\alpha_1\\ \vdots\\ \alpha_N\end{pmatrix} = \begin{pmatrix} b_1\\ \vdots\\ b_N\end{pmatrix}, \tag{20}$$

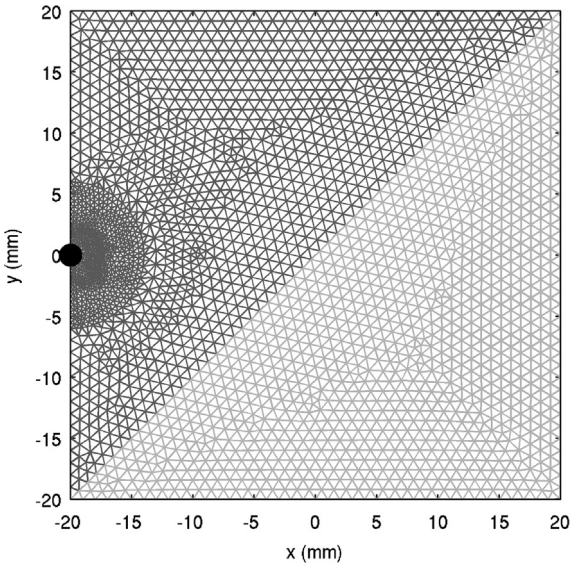

Fig. 4. Mesh for the domain with an oblique surface between the sub-domains with different refractive indices. The sub-domain Ω_1 is marked with dark gray and the sub-domain Ω_2 with light gray. The source is marked with a black circle.

where the vector of radiances in the different sub-domains is $\alpha = (\alpha_1, \ldots, \alpha_N) = (\alpha^1_{1,1}, \ldots, \alpha^1_{1,N_{a,1}}, \ldots, \alpha^1_{N_{s,1},N_{a,1}}, \ldots, \alpha^N_{N_{s,N},N_{a,N}})^T \in \mathbb{C}^{\sum_{k=1}^N N_{s,k}N_{a,k}}$. The matrix $A_k \in \mathbb{C}^{N_{s,k}N_{a,k}\times N_{s,k}N_{a,k}}$ contains the FE-approximation of the RTE in the sub-domain Ω_k

$$A_k = A_{0,k} + A_{1,k} + A_{2,k} + A_{3,k} + A_{4,k}, \tag{21}$$

where

$$A_{0,k}(h,s) = \frac{\mathrm{i}\omega}{c_k}\Bigg(\int_{\Omega_k}\psi_i(\mathbf{r})\psi_j(\mathbf{r})\mathrm{d}r\int_{\mathbb{S}^{d-1}}\psi_l(\hat{\mathbf{s}})\psi_m(\hat{\mathbf{s}})\mathrm{d}\hat{\mathbf{s}} + \int_{\Omega_k}\delta\int_{\mathbb{S}^{d-1}}\hat{\mathbf{s}}\cdot\nabla\psi_j(\mathbf{r})\psi_m(\hat{\mathbf{s}})\psi_l(\hat{\mathbf{s}})\mathrm{d}\hat{\mathbf{s}}\psi_i(\mathbf{r})\mathrm{d}\mathbf{r}\Bigg), \tag{22a}$$

$$A_{1,k}(h,s) = -\int_{\Omega_k}\int_{\mathbb{S}^{d-1}}\hat{\mathbf{s}}\cdot\nabla\psi_j(\mathbf{r})\psi_m(\hat{\mathbf{s}})\psi_l(\hat{\mathbf{s}})\mathrm{d}\hat{\mathbf{s}}\psi_i(\mathbf{r})\mathrm{d}\mathbf{r} + \int_{\Omega_k}\delta\int_{\mathbb{S}^{d-1}}\big(\hat{\mathbf{s}}\cdot\nabla\psi_i(\mathbf{r})\big)\big(\hat{\mathbf{s}}\cdot\nabla\psi_j(\mathbf{r})\big)\psi_l(\hat{\mathbf{s}})\psi_m(\hat{\mathbf{s}})\mathrm{d}\hat{\mathbf{s}}\mathrm{d}\mathbf{r}, \tag{22b}$$

$$A_{2,k}(h,s) = \int_{\partial\Omega_k}\psi_i(\mathbf{r})\psi_j(\mathbf{r})\mathrm{d}S\int_{\mathbb{S}^{d-1}}(\hat{\mathbf{s}}\cdot\hat{\mathbf{n}}_k)_+\psi_l(\hat{\mathbf{s}})\psi_m(\hat{\mathbf{s}})\mathrm{d}\hat{\mathbf{s}} - \int_{\partial\Omega_{k,\mathrm{out}}}\psi_i(\mathbf{r})\psi_j(\mathbf{r})\mathrm{d}S\int_{\mathbb{S}^{d-1}}(\hat{\mathbf{s}}\cdot\hat{\mathbf{n}}_k)_-R_{k,\mathrm{out}}\psi_l(H\hat{\mathbf{s}})\psi_m(\hat{\mathbf{s}})\mathrm{d}\hat{\mathbf{s}} - \int_{\Gamma_{k,n}}\psi_i(\mathbf{r})\psi_j(\mathbf{r})\mathrm{d}S\int_{\mathbb{S}^{d-1}}(\hat{\mathbf{s}}\cdot\hat{\mathbf{n}}_k)_-R_{k,n}\psi_l(H\hat{\mathbf{s}})\psi_m(\hat{\mathbf{s}})\mathrm{d}\hat{\mathbf{s}}, \tag{22c}$$

$$A_{3,k}(h,s) = \int_{\Omega_k}\mu_\mathrm{a}\psi_i(\mathbf{r})\psi_j(\mathbf{r})\mathrm{d}\mathbf{r}\int_{\mathbb{S}^{d-1}}\psi_l(\hat{\mathbf{s}})\psi_m(\hat{\mathbf{s}})\mathrm{d}\hat{\mathbf{s}} + \int_{\Omega_k}\delta\mu_\mathrm{a}\psi_i(\mathbf{r})\int_{\mathbb{S}^{d-1}}\big(\hat{\mathbf{s}}\cdot\nabla\psi_j(\mathbf{r})\big)\psi_m(\hat{\mathbf{s}})\psi_l(\hat{\mathbf{s}})\mathrm{d}\hat{\mathbf{s}}\mathrm{d}\mathbf{r}, \tag{22d}$$

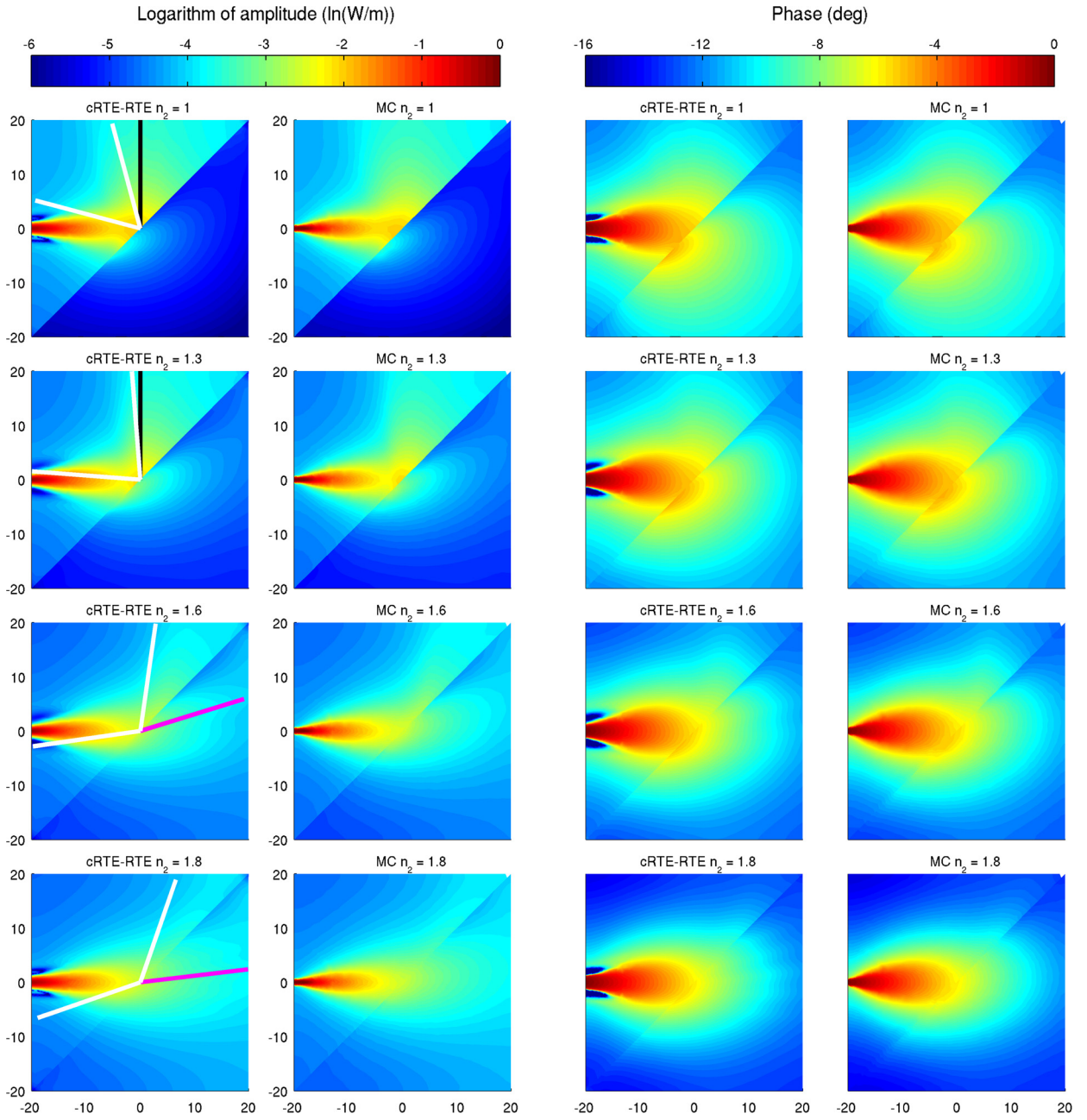

Fig. 5. Logarithm of the amplitude (first and second column) and the phase shift (third and fourth column) of the fluence computed using the cRTE model (first and third column) and using the MC (second and fourth column) due to reflection from the oblique surface. Refractive index of the second sub-domain is $n_2 = 1$ (first row), $n_2 = 1.3$ (second row), $n_2 = 1.6$ (third row) and $n_2 = 1.8$ (fourth row). Directions of reflected and transmitted light with incoming angle of 45 deg are marked with black and purple lines, respectively, and the critical angle is marked with a white line.

$$
\begin{aligned}
A_{4,k}(h,s) = &\int_{\Omega_k} \mu_s \psi_i(\mathbf{r})\psi_j(\mathbf{r})\mathrm{d}\mathbf{r} \int_{\mathbb{S}^{d-1}} \psi_l(\hat{\mathbf{s}})\psi_m(\hat{\mathbf{s}})\mathrm{d}\hat{\mathbf{s}} \\
&+ \int_{\Omega_k} \delta\mu_s \psi_i(\mathbf{r}) \int_{\mathbb{S}^{d-1}} \big(\hat{\mathbf{s}}\cdot\nabla\psi_j(\mathbf{r})\big)\psi_m(\hat{\mathbf{s}})\psi_l(\hat{\mathbf{s}})\mathrm{d}\hat{\mathbf{s}}\mathrm{d}\mathbf{r} \\
&- \int_{\Omega_k} \mu_s \psi_i(\mathbf{r})\psi_j(\mathbf{r})\mathrm{d}\mathbf{r} \int_{\mathbb{S}^{d-1}} \int_{\mathbb{S}^{d-1}} \Theta\big(\hat{\mathbf{s}}\cdot\hat{\mathbf{s}}'\big)\psi_l\big(\hat{\mathbf{s}}'\big)\mathrm{d}\hat{\mathbf{s}}'\psi_m(\hat{\mathbf{s}})\mathrm{d}\hat{\mathbf{s}}
\end{aligned}
$$

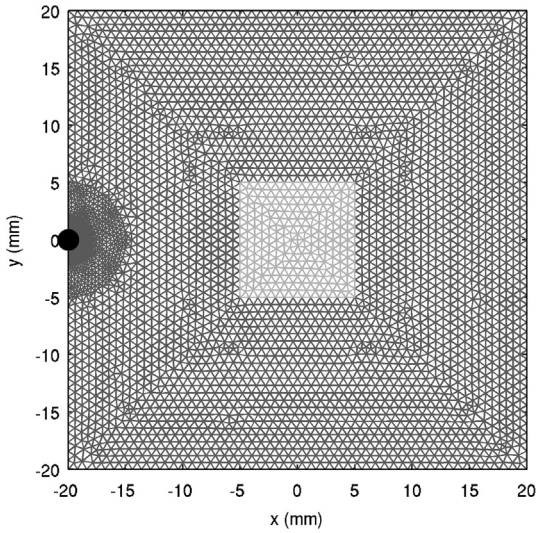

Fig. 6. Mesh for the domain with a square inclusion inside the target. The sub-domain Ω_1 is marked with dark gray and the sub-domain Ω_2 with light gray. The source is marked with a black circle.

$$-\int_{\Omega_k}\delta\mu_s\int_{\mathbb{S}^{d-1}}\left(\hat{\mathbf{s}}\cdot\nabla\psi_j(\mathbf{r})\right)\psi_m(\hat{\mathbf{s}})\int_{\mathbb{S}^{d-1}}\Theta\left(\hat{\mathbf{s}}\cdot\hat{\mathbf{s}}'\right)\psi_l\left(\hat{\mathbf{s}}'\right)\mathrm{d}\hat{\mathbf{s}}'\mathrm{d}\hat{\mathbf{s}}\psi_i(\mathbf{r})\mathrm{d}\mathbf{r}, \tag{22e}$$

where $h=N_{a,k}(j-1)+m$, $s=N_{a,k}(i-1)+l$ ($j,i=1,\ldots,N_{s,k}$, $m,l=1,\ldots,N_{a,k}$, and $h,s=1,\ldots,N_{s,k}N_{a,k}$). Further, the matrix $C_{n,k}\in\mathbb{R}^{N_{s,n}N_{a,n}\times N_{s,k}N_{a,k}}$ contains the coupling conditions on the interface $\Gamma_{k,n}$ due to the radiance transmitted from the sub-domain Ω_n into the sub-domain Ω_k. Note that the matrix $C_{n,k}$ is non-zero only if Ω_n and Ω_k share an interface $\Gamma_{k,n}$. The matrix $C_{n,k}$ can be written as

$$C_{n,k}(p,s)=-\int_{\Gamma_{k,n}}\psi_i(\mathbf{r})\psi_e(\mathbf{r})\mathrm{d}S\int_{\mathbb{S}^{d-1}}(\hat{\mathbf{s}}\cdot\hat{\mathbf{n}}_k)_-T_{n,k}\psi_l\left(K_{n,k}^{-1}(\hat{\mathbf{s}})\right)\psi_u(\hat{\mathbf{s}})\mathrm{d}\hat{\mathbf{s}}, \tag{23}$$

where $p=N_{a,n}(e-1)+u$ ($e=1,\ldots,N_{s,n}$, $u=1,\ldots,N_{a,n}$, and $p=1,\ldots,N_{s,n}N_{a,n}$). The source vector in the sub-domain Ω_k is

$$b_k(h)=\int_{\partial\Omega_{k,\mathrm{out}}}\psi_j(\mathbf{r})\mathrm{d}S\int_{\mathbb{S}^{d-1}}(\hat{\mathbf{s}}\cdot\hat{\mathbf{n}}_k)_-\phi_{0,k}(\mathbf{r},\hat{\mathbf{s}})\psi_m(\hat{\mathbf{s}})\mathrm{d}\hat{\mathbf{s}}. \tag{24}$$

4. Results

The performance of the proposed cRTE model was tested with 2D simulations. The solution of the cRTE was compared with the solution of the Monte Carlo (MC) simulation. In the MC simulations, a photon packet method, originally developed in [53] was modified to allow computation in complex inhomogeneous geometries represented by finite element meshes with piece-wise constant refractive indices [54].

The cRTE was solved using the FEM as described in Section 3. The FE-approximation was computed using Eq. (20). The quantity of interest was the fluence, Eq. (4), inside the domain and at the boundary.

4.1. Reflection from an oblique surface with mismatched refractive indices

First, a reflection from an oblique surface due to a mismatch in the refractive indices was investigated. The simulation domain Ω was a square $[-20,20]\times[-20,20]$ mm^2 shown in Fig. 4. The domain was divided into two sub-domains with different refractive indices. The FE-mesh for the spatial discretization of the sub-domain Ω_1 is marked with dark gray and the sub-domain Ω_2 is marked with light gray in Fig. 4. The FE-meshes consisted of 1710 and 1091 nodes and 3261 and 2043 triangular elements for the sub-domains Ω_1 and Ω_2, respectively. The angular domain $\mathbb{S}^1$ was discretized using 64 equally spaced angular directions for the both sub-domains.

The scattering and absorption properties of the domain were: $\mu_{s,1}=0.1$ mm^{-1}, $\mu_{s,2}=0.1$ mm^{-1}, $\mu_{a,1}=0.01$ mm^{-1}, $\mu_{a,2}=0.01$ mm^{-1}, $g_1=0.8$ and $g_2=0.8$. These values correspond to a low-scattering medium with a forward-peaked scattering. Hence, the reflection from a surface with mismatched refractive indices should be clearly visible. The refractive index of the sub-domain Ω_1 was $n_1=2$ and the refractive index of the sub-domain Ω_2 was given values $n_2=1,1.3,1.6,1.8$.

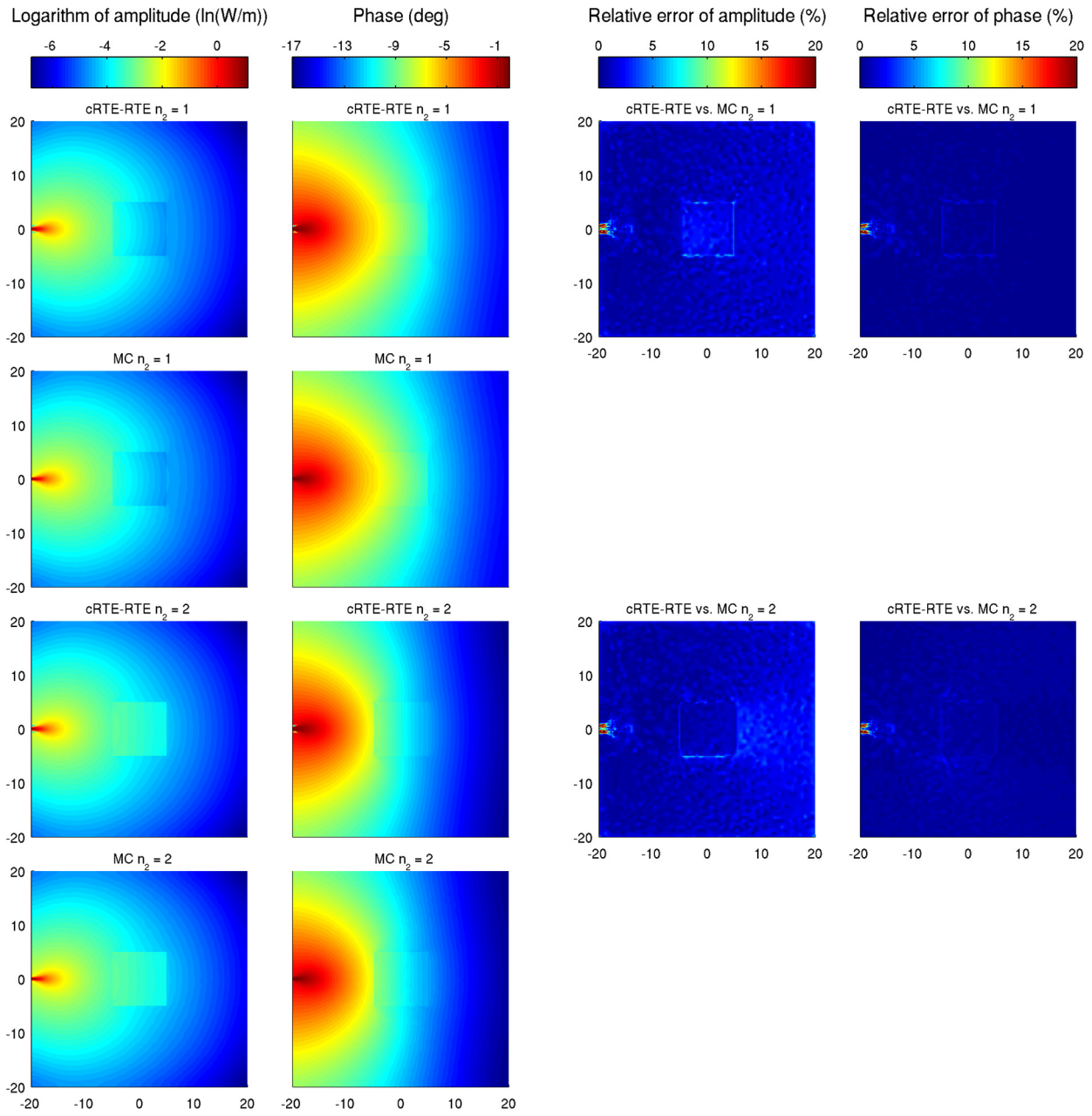

Fig. 7. Logarithm of the amplitude (first column) and the phase shift (second column) of the fluence computed using the cRTE model (first and third row) and using the MC (second and fourth row) due to reflection from the square inclusion inside the target. Refractive index of the inclusion is $n_2 = 1$ (first and second row) and $n_2 = 2$ (third and fourth row). Per cent relative error of the amplitude and the phase shift against the MC are shown in third and fourth columns.

The refractive index of the exterior of the domain Ω was $n_{\text{out}} = 1$. The modulation frequency of the input signal was 100 MHz. A collimated source with a narrow Gaussian angular dependence was located at $(x, y) = (-20, 0)$ mm and it is marked with a black circle in Fig. 4.

The fluence computed using the cRTE and the MC is shown in Fig. 5. As it can be seen, when $n_2 = 1$, most of the light reflects from the surface due a large mismatch in the refractive indices. In this case the critical angle is $\theta_{\text{crit}} = \sin^{-1}(n_2/n_1) = 30$ deg (with respect to the unit normal). This means that only the photons which hit the interface almost perpendicularly can transmit through the interface. Thus, in this case when the medium is low-scattering, most of the photons from the collimated source retain their initial direction before hitting the interface at 45 deg angle and undergo total internal reflection. When the refractive index of the second sub-domain is increased, more light transmits through the surface with a refraction.

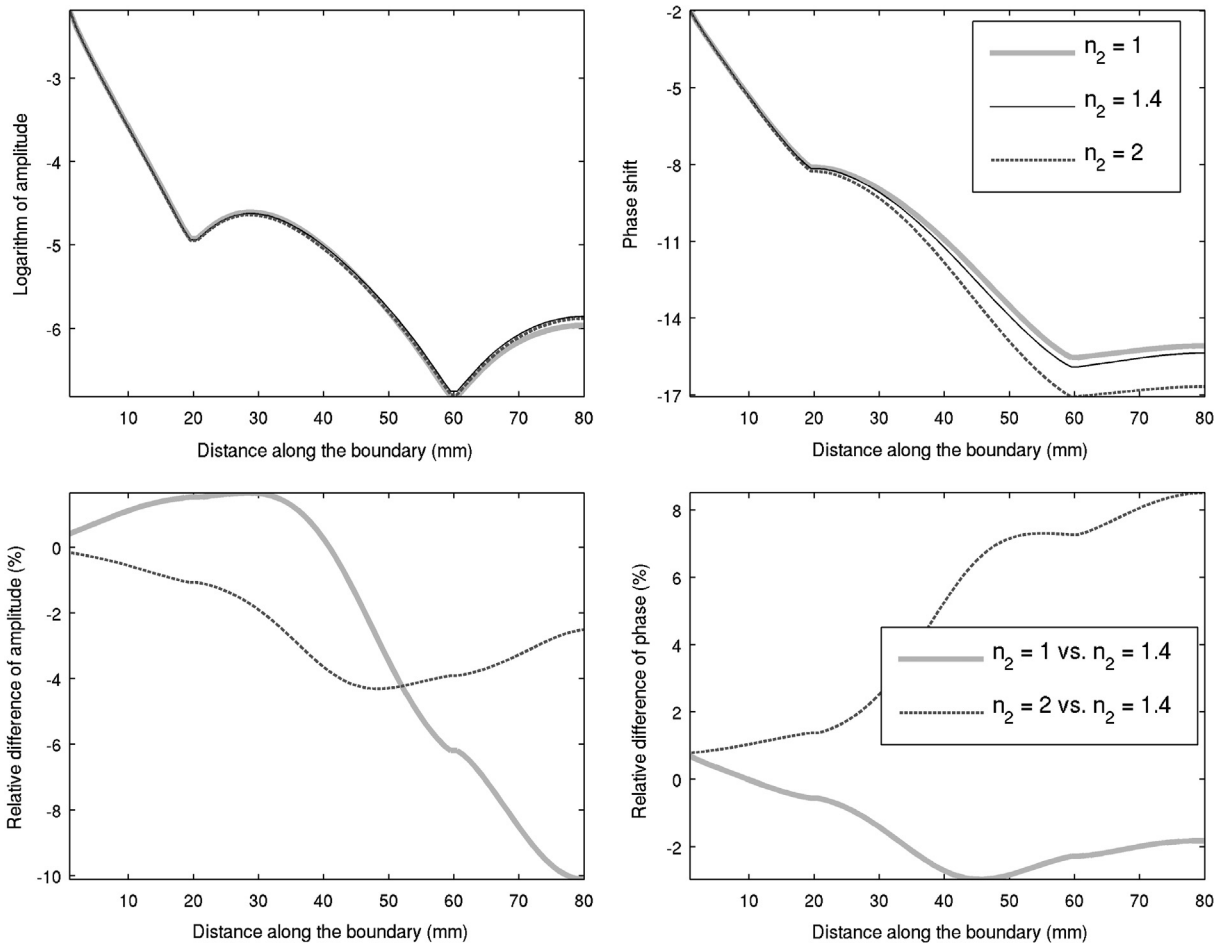

Fig. 8. Logarithm of the amplitude (top left) and the phase shift (top right) of the fluence at the boundary computed using the cRTE model for $n_2 = 1$ (gray line), $n_2 = 1.4$ (black line) and $n_2 = 2$ (dashed line) as a function of distance along the boundary. Per cent relative difference of the amplitude (bottom left) and the phase shift (bottom right) against the case $n_2 = 1.4$ are shown on the bottom row.

When the cRTE and the MC solutions are compared, a good agreement is obtained except close to the source due to different discretization approaches. In the MC, the solution and the source are element-wise constant whereas in the FEM piece-wise linear basis is used. This difference is distinguishable since the medium is small and low-scattering.

4.2. Effect of the internal refractive index change on the boundary measurements

Next, the effect of the internal refractive index change on the boundary measurements was investigated. Two different cases were considered. In the first case, the inclusion with different refractive indices was located deep inside the target and in the second case the inclusion was located close to the boundary of the target.

4.2.1. Inclusion inside the target

First, the inclusion was located inside the target as shown in Fig. 6. The FE-mesh for the spatial discretization of the sub-domain Ω_1 is marked with dark gray and the sub-domain Ω_2 is marked with light gray. The FE-meshes consisted of 3476 and 1051 nodes and 6398 and 1179 triangular elements for the sub-domains Ω_1 and Ω_2, respectively. The angular domain $\mathbb{S}^1$ was discretized using 64 equally spaced angular directions.

The scattering and absorption properties were: $\mu_{s,1} = 1$ mm^{-1}, $\mu_{s,2} = 1$ mm^{-1}, $\mu_{a,1} = 0.01$ mm^{-1}, $\mu_{a,2} = 0.01$ mm^{-1}, $g_1 = 0.8$ and $g_2 = 0.8$. The refractive index of the sub-domain Ω_1 was $n_1 = 1.4$ and the refractive index of the sub-domain Ω_2 was $n_2 = 1, 1.05, \ldots, 2$. The refractive index of the exterior was $n_{\text{out}} = 1$.

The fluences computed using the cRTE and the MC are shown in Fig. 7. In addition, per cent relative error of the fluence computed using the cRTE against the MC is shown. Fig. 8 shows the fluence at the boundary computed using the cRTE for $n_2 = 1$ (gray line), $n_2 = 1.4$ (black line) and $n_2 = 2$ (dashed line) as a function of distance along the boundary. In addition, per cent relative difference against the case with $n_2 = 1.4$ (matched refractive indices) is shown. The mean of the relative

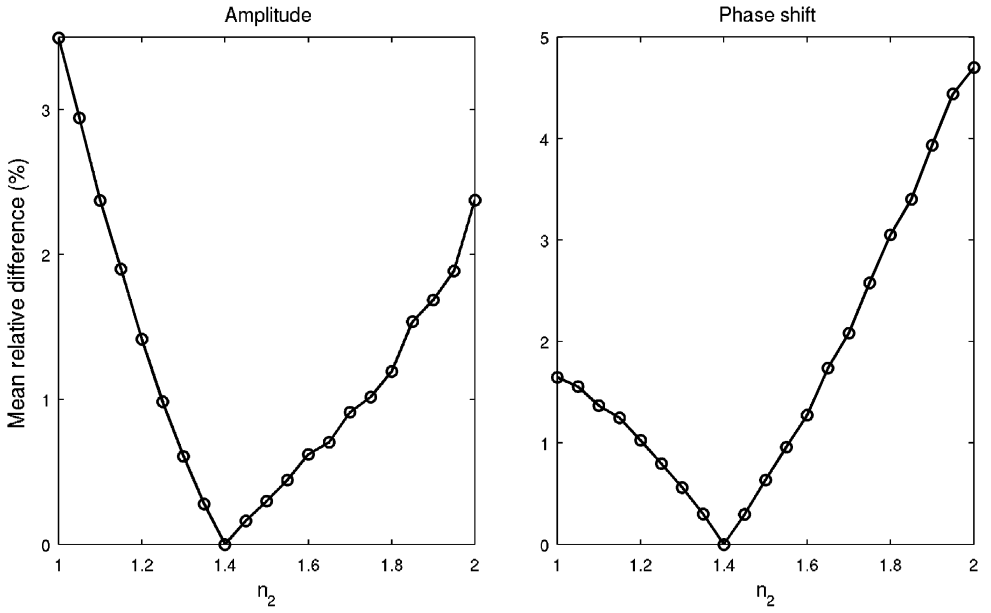

Fig. 9. Mean per cent relative difference of the amplitude (left) and the phase shift (right) of the fluence at the boundary as a function of refractive index of the inclusion n_2.

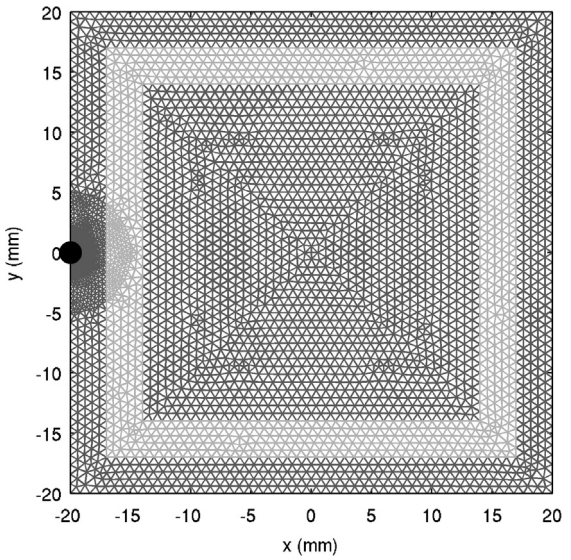

Fig. 10. Mesh for the domain with a layer inclusion close to the boundary of the domain. The sub-domain Ω_1 is marked with dark gray and the sub-domain Ω_2 with light gray. The source is marked with a black circle.

difference of the boundary measurements against the case with $n_2 = 1.4$ was computed for the amplitude and for the phase as

$$\Delta_{|\Phi|} = \text{mean}\left(\left|\frac{|\Phi(\mathbf{r})| - |\Phi_{\text{ref}}(\mathbf{r})|}{|\Phi_{\text{ref}}(\mathbf{r})|}\right|\right), \tag{25}$$

$$\Delta_{\arg(\Phi)} = \text{mean}\left(\left|\frac{\arg(\Phi(\mathbf{r})) - \arg(\Phi_{\text{ref}}(\mathbf{r}))}{\arg(\Phi_{\text{ref}}(\mathbf{r}))}\right|\right), \tag{26}$$

where $\Phi_{\text{ref}}(\mathbf{r})$ is the solution with $n_2 = 1.4$, $|\cdot|$ is the absolute value and $\arg(\cdot)$ is the phase angle. This quantity is shown in Fig. 9 for the amplitude (left image) and for the phase (right image).

The results in Fig. 7 show that when the refractive index of the inclusion is lower ($n_2 = 1$) than the refractive index of the background ($n_1 = 1.4$) strong reflection occurs when light enters the inclusion. In contrast, when the refractive index is larger ($n_2 = 2$) than that of the background, more light is transmitted into the inclusion and total internal reflection takes

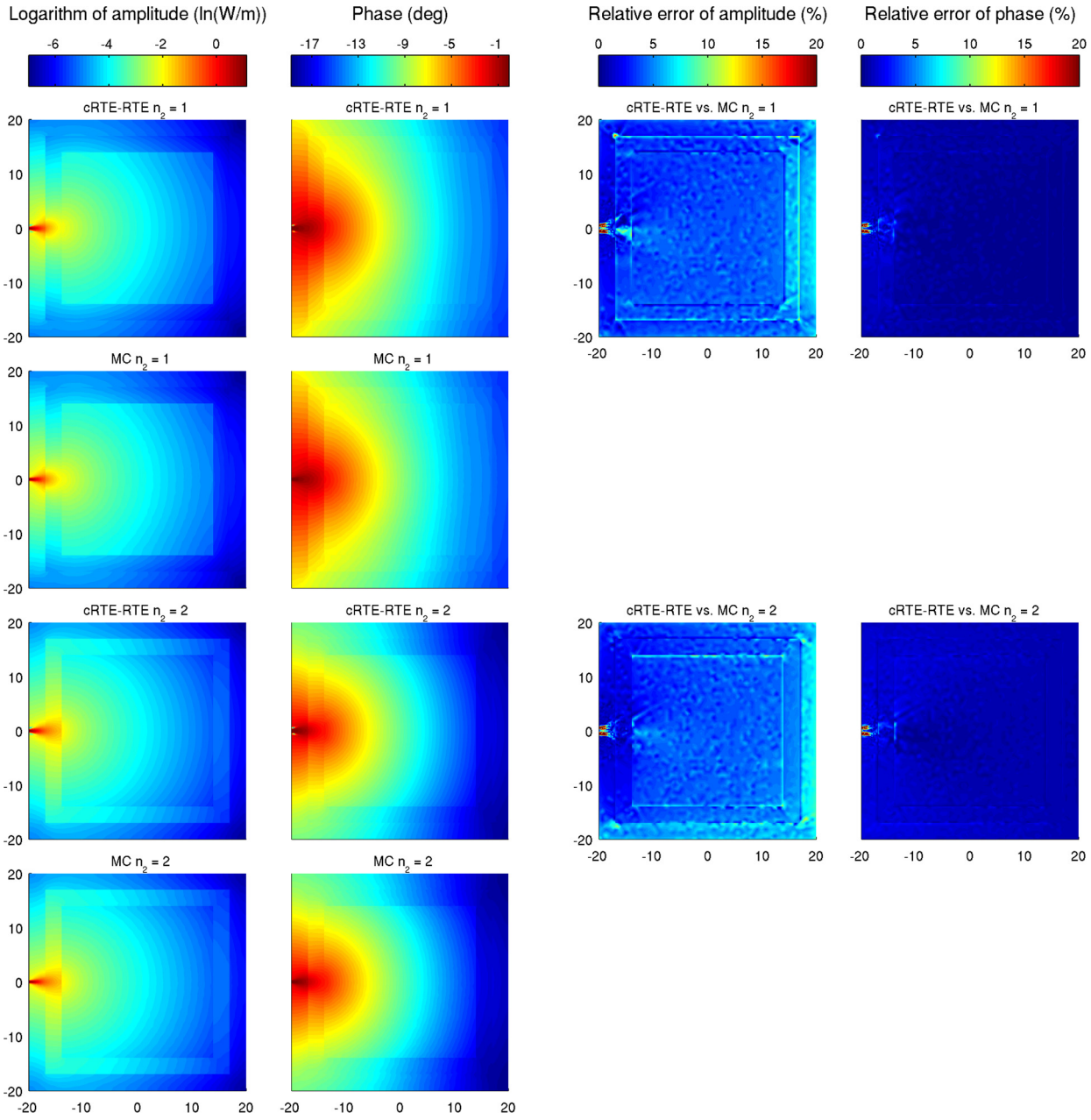

Fig. 11. Logarithm of the amplitude (first column) and the phase shift (second column) of the fluence computed using the cRTE model (first and third row) and using the MC (second and fourth row) due to reflection from the layer inclusion close to the boundary of the target. Refractive index of the inclusion is $n_2 = 1$ (first and second row) and $n_2 = 2$ (third and fourth row). Per cent relative error of the amplitude and the phase shift against the MC are shown in third and fourth columns.

place when light exits the inclusion. When the cRTE and the MC solutions are compared, a very good agreement is found and the relative error is under three per cent for both the amplitude and the phase further from the source.

The results show that the fluence at the boundary is changed when the refractive index is not constant within the target. When the refractive index of the inclusion is lower ($n_2 = 1$) than that of the background, larger values for the amplitude can be measured next to the source due to the reflection from the inclusion. At the opposite side of the target, the amplitude is up to 10% lower compared to the fluence without the inclusion. For the phase, smaller values can be measured next to the source since photons can arrive earlier to the boundary due to the possible reflection. If the refractive index is larger ($n_2 = 2$) than that of the background, the amplitude is one to four per cent lower compared to the fluence obtained without the inclusion. For the phase, up to 8% larger values are obtained since photons can arrive later to the boundary due to the internal reflection inside the inclusion.

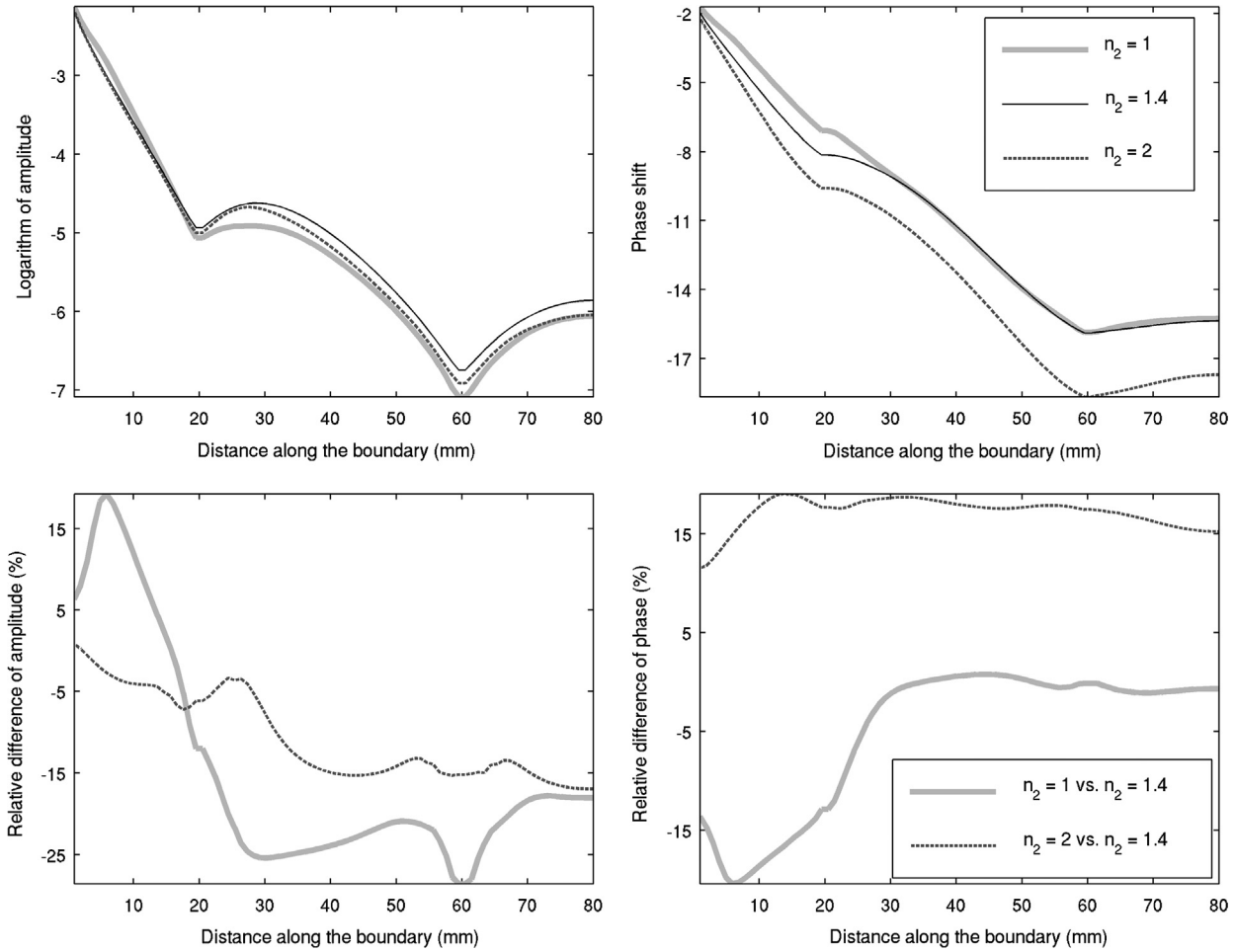

Fig. 12. Logarithm of the amplitude (top left) and the phase shift (top right) of the fluence at the boundary computed using the cRTE model for $n_2 = 1$ (gray line), $n_2 = 1.4$ (black line) and $n_2 = 2$ (dashed line) as a function of distance along the boundary. Per cent relative difference of the amplitude (bottom left) and the phase shift (bottom right) against the case $n_2 = 1.4$ are shown on the bottom row.

4.2.2. Inclusion close to the boundary of the target

In the second case, the inclusion located close to the boundary of the target as shown in Fig. 10. The number of spatial and angular nodes and elements were the same as before. In addition, the scattering and absorption properties were the same as in the first case in Section 4.2.1. Again, we set the refractive index of the background to $n_1 = 1.4$ and varied the refractive index of the layer n_2.

The fluences computed using the cRTE and the MC are shown in Fig. 11 for $n_2 = 1$ and for $n_2 = 2$. In addition, per cent relative error of the fluence computed using the cRTE is shown. Fig. 12 shows the fluence at the boundary for $n_2 = 1$, $n_2 = 1.4$ and for $n_2 = 2$. The mean of the relative difference of the boundary measurements against the case with $n_2 = 1.4$ (matched refractive indices) is shown in Fig. 13.

The results in Fig. 11 show that for a smaller refractive index value ($n_2 = 1$) strong reflection occurs in front of the source when light enters the layer. As a result, a major portion of light remains between the layer and the boundary of the target. In addition, the part of the light which is transmitted through the layer in the front of the source gets reflected at the opposite side of the layer. Hence, some part of the light remains trapped inside the inner boundary of the layer. In contrast, for a larger refractive index ($n_2 = 2$) more light is transmitted into the layer and light propagates along the layer. This is due the total internal reflection. The cRTE and the MC solutions agree relative well even though some differences can be seen at the right-hand side of the target between the layer and the boundary of the target.

The results in Fig. 12 show that up to 15% larger and 25% smaller values can be measured for the amplitude next to the source and at the opposite side of the target, respectively, when the refractive index n_2 is smaller than the background in comparison to the fluences computed without the inclusion. For the phase, up to 15% difference can be obtained. Based on the results it can be concluded that if the internal refractive index change occurs close to the boundary, significant changes in the boundary measurements can be obtained.

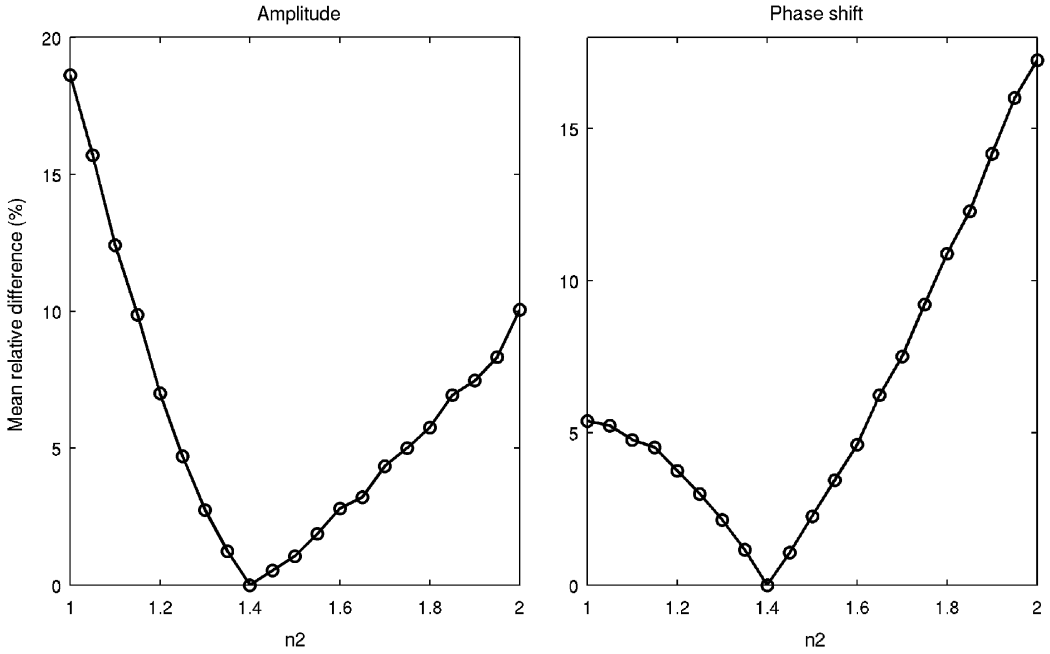

Fig. 13. Mean per cent relative difference of the amplitude (left) and the phase shift (right) of the fluence at the boundary as a function of refractive index of the layer n_2.

5. Conclusions

In this work, light propagation in a scattering medium with piece-wise constant refractive index using the radiative transport equation was studied. Light propagation in each sub-domain with a constant refractive index was modeled using the RTE and the equations were coupled using boundary conditions describing Fresnel reflection and transmission phenomenas on the interfaces between the sub-domains. The resulting coupled system of RTEs was numerically solved using the FEM. The proposed model was tested using simulations and was compared with the solution of the Monte Carlo method. The results show that the coupled RTE model describes light propagation accurately in comparison with the Monte Carlo method. In addition, results show that neglecting internal refractive index changes can lead to erroneous boundary measurements of scattered light. This indicates that the quality of the DOT reconstructions could possible be increased by incorporating a model for internal refractive index changes in the image reconstruction procedure.

Acknowledgements

The authors would like to thank Aki Pulkkinen for providing the Monte Carlo simulation solver. This work has been supported by the Academy of Finland (projects 136220, 140984, and 250215 Finnish Centre of Excellence in Inverse Problems Research), Finnish Doctoral Programme in Computational Sciences (FICS), Magnus Ehrnrooth Foundation, the strategic funding of the University of Eastern Finland, and by EPSRC grants GR/R86201/01 and EP/E034950/1.

References

[1] S. Chandrasekhar, Radiative Transfer, Oxford University Press, London, 1950.
[2] K. Case, P. Zweifel, Linear Transport Theory, Addison–Wesley Educational Publishers Inc., US, 1967.
[3] A. Ishimaru, Wave Propagation and Scattering in Random Media, Academic Press/IEEE Press, New York, 1978.
[4] G.E. Thomas, K. Stamnes, Radiative Transfer in the Atmosphere and Ocean, Cambridge University Press, 2002.
[5] G.B. Rybicki, A.P. Lightman, Radiative Processes in Astrophysics, John Wiley & Sons, 2008.
[6] E.E. Lewis, W.F. Miller, Computational Methods of Neutron Transport, John Wiley and Sons, Inc., New York, NY, 1984.
[7] L. Wang, H. Wu, Biomedical Optics: Principles and Imaging, Wiley–Blackwell, 2007.
[8] S. Arridge, Optical tomography in medical imaging, Inverse Probl. 15 (1999) R41.
[9] S. Arridge, J. Schotland, Optical tomography: forward and inverse problems, Inverse Problems 25 (2009) 123010.
[10] G. Bal, Inverse transport theory and applications, Inverse Problems 25 (2009) 053001, 48 pp.
[11] S. Arridge, Methods in diffuse optical imaging, Philos. Trans. R. Soc. A, Math. Phys. Eng. Sci. 369 (2011) 4558–4576.
[12] G.C. Pomraning, The Equations of Radiation Hydrodynamics, Courier Dover Publications, 1973.
[13] H. Ferwerda, The radiative transfer equation for scattering media with a spatially varying refractive index, J. Opt. A, Pure Appl. Opt. 1 (1999) L1–L2.
[14] J.-M. Tualle, E. Tinet, Derivation of the radiative transfer equation for scattering media with a spatially varying refractive index, Opt. Commun. 228 (2003) 33–38.
[15] L. Martí-López, J. Bouza-Domínguez, J. Hebden, S. Arridge, R. Martín, Validity conditions for the radiative transfer equation, J. Opt. Soc. Am. A 20 (2003) 2046–2056.

[16] M.L. Shendeleva, Radiative transfer in a turbid medium with a varying refractive index: comment, J. Opt. Soc. Am. A 21 (2004) 2464–2467.
[17] M. Premaratne, E. Premaratne, A.J. Lowery, The photon transport equation for turbid biological media with spatially varying isotropic refractive index, Opt. Express 13 (2005) 389–399.
[18] L. Martí-López, J. Bouza-Domínguez, R. Martínez-Celorio, J. Hebden, An investigation of the ability of modified radiative transfer equations to accommodate laws of geometrical optics, Opt. Commun. 266 (2006) 44–49.
[19] G. Bal, Radiative transfer equations with varying refractive index: a mathematical perspective, J. Opt. Soc. Am. A 23 (2006) 1639–1644.
[20] J.-M. Tualle, Link between the laws of geometrical optics and the radiative transfer equation in media with a spatially varying refractive index, Opt. Commun. 281 (2008) 3631–3635.
[21] J. Boulanger, O. Balima, A. Charette, Refractive index imaging from radiative transfer equation-based reconstruction algorithm: fundamentals, J. Quant. Spectrosc. Radiat. Transf. 112 (2011) 1222–1228.
[22] J. Cassell, M. Williams, Radiation transport and internal reflection in a sphere, J. Quant. Spectrosc. Radiat. Transf. 101 (2006) 16–28.
[23] J. Cassell, M. Williams, Radiation transport and internal reflection in a two region, turbid sphere, J. Quant. Spectrosc. Radiat. Transf. 104 (2007) 400–427.
[24] Z. Jin, K. Stamnes, Radiative transfer in nonuniformly refracting layered media: atmosphere–ocean system, Appl. Opt. 33 (1994) 431–442.
[25] R. Elaloufi, S. Arridge, R. Pierrat, R. Carminati, Light propagation in multilayered scattering media beyond the diffusive regime, Appl. Opt. 46 (2007) 2528–2539.
[26] R. Garcia, C. Siewert, A. Yacout, On the use of Fresnel boundary and interface conditions in radiative-transfer calculations for multilayered media, J. Quant. Spectrosc. Radiat. Transf. 109 (2008) 752–769.
[27] B. Bulgarelli, V.B. Kisselev, L. Roberti, Radiative transfer in the atmosphere–ocean system: the finite-element method, Appl. Opt. 38 (1999) 1530–1542.
[28] K.G. Phillips, S.L. Jacques, Solution of transport equations in layered media with refractive index mismatch using the P_N-method, J. Opt. Soc. Am. A 26 (2009) 2147–2162.
[29] O. Dorn, A transport–backtransport method for optical tomography, Inverse Problems 14 (1998) 1107–1130.
[30] A. Hielscher, R. Alcouffe, R. Barbour, Comparison of finite-difference transport and diffusion calculations for photon migration in homogeneous and heterogeneous tissues, Phys. Med. Biol. 43 (1998) 1285–1302.
[31] J. Boulanger, A. Charette, Reconstruction optical spectroscopy using transient radiative transfer equation and pulsed laser: a numerical study, J. Quant. Spectrosc. Radiat. Transf. 93 (2005) 325–336.
[32] G. Kanschat, A robust finite element discretization for radiative transfer problems with scattering, East-West J. Numer. Math. 6 (1998) 265–272.
[33] G. Abdoulaev, A. Hielscher, Three-dimensional optical tomography with the equation of radiative transfer, J. Electron. Imaging 12 (2003) 594.
[34] T. Tarvainen, M. Vauhkonen, V. Kolehmainen, J. Kaipio, Hybrid radiative-transfer-diffusion model for optical tomography, Appl. Opt. 44 (2005) 876–886.
[35] H. Gao, H. Zhao, A fast-forward solver of radiative transfer equation, Transp. Theory Stat. Phys. 38 (2009) 149–192.
[36] K. Ren, G. Abdoulaev, G. Bal, A. Hielscher, Algorithm for solving the equation of radiative transfer in the frequency domain, Opt. Lett. 29 (2004) 578–580.
[37] K. Ren, G. Bal, A. Hielscher, Frequency domain optical tomography based on the equation of radiative transfer, SIAM J. Sci. Comput. 28 (2006) 1463–1489.
[38] F. Asllanaj, S. Fumeron, Applying a new computational method for biological tissue optics based on the time-dependent two-dimensional radiative transfer equation, J. Biomed. Opt. 17 (2012) 075007, 11 pp.
[39] J. Tervo, P. Kolmonen, M. Vauhkonen, L.M. Heikkinen, J.P. Kaipio, A finite-element model of electron transport in radiation therapy and a related inverse problem, Inverse Problems 15 (1999) 1345.
[40] E. Boman, J. Tervo, M. Vauhkonen, Modelling the transport of ionizing radiation using the finite element method, Phys. Med. Biol. 50 (2005) 265–280.
[41] T. Tarvainen, V. Kolehmainen, S.R. Arridge, J.P. Kaipio, Image reconstruction in diffuse optical tomography using the coupled radiative transport–diffusion model, J. Quant. Spectrosc. Radiat. Transf. 112 (2011) 2600–2608.
[42] E. Aydin, C. De Oliveira, A. Goddard, A comparison between transport and diffusion calculations using a finite element-spherical harmonics radiation transport method, Med. Phys. 29 (2002) 2013.
[43] S. Wright, M. Schweiger, S. Arridge, Reconstruction in optical tomography using the P_N approximations, Meas. Sci. Technol. 18 (2007) 79–86.
[44] P.S. Mohan, T. Tarvainen, M. Schweiger, A. Pulkkinen, S.R. Arridge, Variable order spherical harmonic expansion scheme for the radiative transport equation using finite elements, J. Comput. Phys. 230 (2011) 7364–7383.
[45] K. Grella, C. Schwab, Sparse tensor spherical harmonics approximation in radiative transfer, J. Comput. Phys. 230 (2011) 8452–8473.
[46] L. Henyey, J. Greenstein, Diffuse radiation in the Galaxy, Astrophys. J. 93 (1941) 70–83.
[47] T. Tarvainen, M. Vauhkonen, V. Kolehmainen, J. Kaipio, Finite element model for the coupled radiative transfer equation and diffusion approximation, Int. J. Numer. Methods Eng. 65 (2006) 383–405.
[48] T. Tarvainen, M. Vauhkonen, V. Kolehmainen, S. Arridge, J. Kaipio, Coupled radiative transfer equation and diffusion approximation model for photon migration in turbid medium with low-scattering and non-scattering regions, Phys. Med. Biol. 50 (2005) 4913–4930.
[49] O. Lehtikangas, T. Tarvainen, A. Kim, Modeling boundary measurements of scattered light using the corrected diffusion approximation, Biomed. Opt. Express 3 (2012) 552–571.
[50] O. Lehtikangas, T. Tarvainen, Hybrid forward-peaked-scattering–diffusion approximations for light propagation in turbid media with low-scattering regions, J. Quant. Spectrosc. Radiat. Transf. 116 (2013) 132–144.
[51] G. Arfken, Mathematical Methods for Physicists, Academic Press, New York, 1985.
[52] S. Richling, E. Meinköhn, N. Kryzhevoi, G. Kanschat, Radiative transfer with finite elements, Astron. Astrophys. 380 (2001) 776–788.
[53] S. Prahl, M. Keijzer, S. Jacques, A. Welch, A Monte Carlo model of light propagation in tissue, in: SPIE Proceedings of Dosimetry of Laser Radiation in Medicine and Biology, 1989, pp. 102–111.
[54] T. Tarvainen, V. Kolehmainen, A. Pulkkinen, M. Vauhkonen, M. Schweiger, S. Arridge, J. Kaipio, An approximation error approach for compensating for modelling errors in DOT, Inverse Problems 26 (2010) 015005.